Purity and efficiency of hybrid orbital angular momentum-generating metasurfaces

Bereneice Sephton
Yao-Wei Huang
Antonio Ambrosio
Cheng-Wei Qiu
Adam Vallés
Takashige Omatsu
Frederico Capasso
Andrew Forbes

Purity and efficiency of hybrid orbital angular momentum-generating metasurfaces

Bereneice Sephton,[a] Yao-Wei Huang,[b,c] Antonio Ambrosio,[b,d] Cheng-Wei Qiu,[c] Adam Vallés,[a,e] Takashige Omatsu,[e,f] Frederico Capasso,[b] and Andrew Forbes[a,*]

[a]University of the Witwatersrand, School of Physics, Johannesburg, South Africa
[b]Harvard University, Harvard John A. Paulson School of Engineering and Applied Sciences, Cambridge, Massachusetts, United States
[c]National University of Singapore, Department of Electrical and Computer Engineering, Singapore
[d]Fondazione Istituto Italiano di Tecnologia, Milano, Italy
[e]Chiba University, Molecular Chirality Research Center, Inage-ku, Chiba, Japan
[f]Chiba University, Graduate School of Advanced Integration Science, Inage-ku, Chiba, Japan

Abstract. Controlling light with subwavelength-designed metasurfaces (MSs) has allowed for the arbitrary creation of structured light by precisely engineered matter. We report on the purity and conversion efficiency of hybrid orbital angular momentum (OAM)-generating MSs. We use a recently reported method to design and fabricate meta-surfaces that exploit generalized spin-orbit coupling to produce vector OAM states with asymmetric OAM superpositions, e.g., 1 and 5, coupled to linear and circular polarization states, fractional vector OAM states with OAM values of 3.5 and 6.5, and also the common conjugate spin and OAM of ± 1 as reported in previous spin-orbit coupling devices. The OAM and radial modes in the resulting beams are quantitatively studied by implementing a modal decomposition approach, establishing both purity and conversion efficiency. We find conversion efficiencies exceeding 75% and purities in excess of 95%. A phase-flattening approach reveals that the OAM purity can be very low due to the presence of undesired radial components. We characterize the effect and illustrate how to suppress the undesired radial modes. © *2020 Society of Photo-Optical Instrumentation Engineers (SPIE)* [DOI: 10.1117/1.JNP.14.016005]

1 Introduction

Twisting the phase front of light so that it varies azimuthally as $\exp(i\ell\phi)$ is well known to generate orbital angular momentum (OAM), with $\ell\hbar$ imparted per photon,[1] where ϕ is the azimuthal angle. Classically, this is seen as the wavefront comprising ℓ-intertwined helices and a phase singularity in the center. Exploiting this property of structured light has resulted in a versatile range of classical and quantum applications, forming a basis for communication,[2–4] quantum cryptography,[5] surface microstructure processing,[6,7] and the synthesis of helical microfibers.[8] Furthermore, pairing different OAM modes with orthogonal polarization in a non-separable manner produces vector beams, allowing for smaller beam waists in optical tweezing,[9,10] additional applications in optical microscopy,[11,12] implementation of quantum walks,[13,14] classical error correction of quantum channels,[15] and another resource for quantum memory.[16]

It follows that straightforward, simple generation of such OAM beams is largely advantageous for implementation into systems with minimal effort and has precipitated work on

---

*Address all correspondence to Andrew Forbes, E-mail: andrew.forbes@wits.ac.za

various devices to accomplish this. Originally this was achieved through alteration of the dynamic phase by either varying the path length with the thickness of a transparent medium (spiral phase plate)[17] or varying the refractive index with the orientation of liquid crystal (LC) molecules [LC spatial light modulators (SLMs)].[18,19] Nonetheless, dynamic phase requires involved interferometric methods to generate vector vortex beams, adding complexity for incorporation of these beams into experiments. Exploitation of geometric phase in 2006 with the advent of the q-plate (QP),[20] however, quickly simplified the generation process for both scalar OAM modes and vector vortex beams. This is made possible as polarization or spin angular momentum (SAM) and OAM couples in an optically inhomogeneous, anisotropic medium such as LC molecules patterned in a particular way. Here OAM of $\pm 2q$ is generated for an SAM input of right- or left-handed circular polarization (CP), where q is the topological charge related to the LC pattern. As polarization is used to control the OAM generated, a single mode of the complex conjugate set $(\pm 2q)$ is easily generated by simply selecting the input beam polarization. In addition, traversal of the device with a superposition of the CP states yields a vector vortex beam with a nonseparable pairing of CP and OAM in the mode generated; this hugely simplifies the experimental creation and implementation of these beams.

The generation of geometric phase, however, is not limited to LCs and thus may also be applied to metasurfaces (MSs).[21–24] In addition, by utilizing MSs, one can realize a higher resolution for the encoded phase pattern due to the smaller fins, allowing for increased versatility. Specifically, the OAM-to-polarization pairing may be made arbitrary such that the OAM charges need not be complex conjugates of each other,[25] the controlling polarization basis may also be made arbitrary, e.g., linear instead of circular[26] and as MSs can withstand more power, the devices have, in principle, higher energy thresholds.[27]

Here we fabricated metasurfaces, exploiting geometric phase to engineer arbitrary hybrid OAM modes. Our devices generate OAM charges of 3 and 6 with CP, as well as charges ± 1 along with 1 and 5 with linear polarization. Furthermore, we extend the possibilities to include the generation of fractional charges, 3.5 and 6.5, from incident CP. Employing these elements experimentally, we generate these modes and analyze their operation using a phase-flattening approach.[28–31] This gives a greater quantitative measure of the performance than the often-used interferometric method whereby a fork or spiral interference pattern is created.[22,25,26,32–34] By utilizing this analysis tool, we are able to explicitly show a full breakdown of the modal content for the beams generated, including that of the radial distribution, which is usually ignored. The proper configuration of laser cavities for the direct generation of spatial modes as an eigenmode[35–38] has been the most commonly used technique to date, avoiding the generation of undesired radial components. We show in this work an example of how an amplitude-phase modulation also allows for high purity OAM mode generation. Moreover, we are able to precisely define and separate the modal purity and efficiency of the devices, which may be conveniently determined by analyzing the same results.

2 Theory

2.1 *Metasurfaces for Hybrid OAM Modes*

Geometric or Pancharatnam–Berry phase[39,40] has become a well-used property due to its ability to couple polarization to OAM and thus allows control of a degree of freedom with another. By transforming polarization so that it undergoes a change of states that forms a closed loop on the Poincaré sphere, an associated phase equal to half the area enclosed by the path made by the transformation is introduced to the light.[39] Accordingly, by making this state change vary spatially across the transverse profile of a beam, a spatially varying phase can be engineered[41] such as in the azimuthal direction with OAM generation.[20]

Owing to the freedom of fashioning the width, length, and orientation of the MSs patterned across the device, one can control the geometric phase of the light traversing the material. Increased liberty is, thus, afforded in terms of the polarization bases that can be manipulated and the resulting OAM modes generated.[26] As such, the total angular momentum is manipulated

with this device, which is termed J-plate (JP). Using the Jones matrix formalism in the linear polarization basis, the JP transformation may be described as[26]

$$J(\phi) = \begin{vmatrix} e^{i\delta}[e^{im\phi}\cos^2(\chi) + e^{in\phi}\sin^2(\chi)] & \frac{\sin(2\chi)}{2}(e^{im\phi} - e^{in\phi}) \\ \frac{\sin(2\chi)}{2}(e^{im\phi} - e^{in\phi}) & e^{-i\delta}[e^{im\phi}\sin^2(\chi) + e^{in\phi}\cos^2(\chi)] \end{vmatrix}, \quad (1)$$

where ϕ is the azimuthal angle, n and m are the integer values, and χ and δ are the angles dictating the polarization state.

The generalized input polarization basis states are thus,

$$|\lambda^+\rangle = \begin{vmatrix} \cos(\chi) \\ e^{i\delta}\sin(\chi) \end{vmatrix} \quad (2)$$

and

$$|\lambda^-\rangle = \begin{vmatrix} -\sin(\chi) \\ e^{i\delta}\cos(\chi) \end{vmatrix}. \quad (3)$$

The JP then carries out the operations: $|\lambda^+\rangle \rightarrow e^{im\phi}|(\lambda^+)^*\rangle$ and $|\lambda^-\rangle \rightarrow e^{in\phi}|(\lambda^-)^*\rangle$, with $*$ indicating the complex conjugate. Accordingly, the phase front of the beam acquires a factor of $e^{im\phi}$ ($e^{in\phi}$) for the basis polarization state $|\lambda^+\rangle$ ($|\lambda^-\rangle$). The beam then obtains m (n) twists in the phase front, corresponding to an OAM of $m\hbar$ ($n\hbar$) per photon, and a change in the polarization state to its complex conjugate.

Q-plates subsequently form a subset of these operations where $\chi = \pi/4$ and $\delta = \pi/2$ as the polarization basis are restricted to circular polarized states ($|\lambda^+\rangle = |L\rangle$ and $|\lambda^-\rangle = |R\rangle$) with $m = -n$ as the generated OAM must be complex conjugates.[20,21] In the case of our MSs, however, paired control of the polarization basis along with the generated OAM is arbitrary, allowing the generation of hybrid OAM modes, including the generation of fractional states.
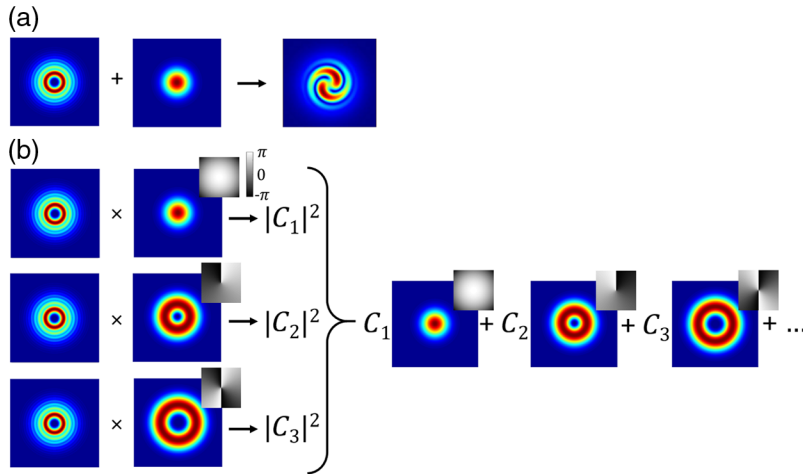
2.2 Modal Decomposition

Traditionally, the operation of such devices are tested by interfering a reference Gaussian beam and the generated mode (test beam) to yield a spiral interference pattern, as depicted in Fig. 1(a). The arms in the resultant spiral interferogram realizes the twisted phase front in the intensity distribution with the number of arms in the pattern indicating the OAM carried in the test beam. Here the two arms indicate that a charge of $\ell = 2$ is carried by the generated beam on the right. It follows that this forms a more qualitative test on the OAM content as smaller amounts of other OAM modes would not be clearly indicated by the interferogram. A well-researched technique is available, however, where the reciprocity of light is harnessed to quantitatively look at the generated modes. The concept thereof is shown in Fig. 1(b). It allows one to not only determine the modal content of an arbitrary beam, and thus the purity of the mode generated, but also determine the efficiency at which the conversion takes place. To do so, we express the generated field $E(r, \phi)$ in a set of orthogonal basis modes, such as the Laguerre–Gaussian modes, $\mathrm{LG}_{p,\ell}(r, \phi)$:[28,29]

$$E(r, \phi) = \sum_{p,\ell} C_{p,\ell} \mathrm{LG}_{p,\ell}(r, \phi), \quad (4)$$

where $C_{p,\ell} = \rho_{p,\ell} e^{i\Delta\varphi_{p,\ell}}$ is the complex correlation coefficient that weights the contributions of each basis mode ($\mathrm{LG}_{p,\ell}$). Here $\rho_{p,\ell}$ is the associated amplitude and $\Delta\varphi_{p,\ell}$ is the phase between the ($LG_{p,\ell}$)'th mode and an arbitrary reference (often $p = 0$, $\ell = 0$) and

$$\mathrm{LG}_{p,\ell}(r, \phi) = \sqrt{\frac{2p!}{\pi w_0^2(p + |\ell|)!}} \left(\frac{r\sqrt{2}}{w_0}\right)^{|\ell|} L_p^{|\ell|}\left(\frac{2r^2}{w_0^2}\right) e^{-\frac{r^2}{w_0^2}} e^{-i\ell\phi} \quad (5)$$

at the beam waist ($w = w_0$). Here (r, ϕ) are the radial and azimuthal coordinates in the transverse plane, ℓ is the OAM index, $p \geq 0$ is the radial index indicating the number of intensity

Fig. 1 A conceptual depiction of the processes and types of data typically obtained by utilizing the (a) interference and (b) modal decomposition approach for the analysis of a generated mode (right) by exploiting the known Laguerre–Gaussian modes (left of multiplication sign).

nulls in the radial profile, and $L_p^{|\ell|}(x)$ is the Laguerre polynomial of orders p, ℓ. This expansion in a basis mode set is not limited to LG modes, however, but can be done in any basis such as Ince–Gaussian or Bessel–Gaussian. The choice of LG modes served to simplify the analysis.

Quantitative determination of the generated beam purity may, thus, be achieved by decomposing it into individual modes by determination of the basis mode weightings, $|C_{p,\ell}|^2$. A phase-flattening approach may be taken whereby an inner product of the generated field and the mode being decomposed into are formed:[30,31]

$$C_{p,\ell} = \langle \mathrm{LG}_{p,\ell}(r,\phi)|E(r,\phi)\rangle = \iint_{R^2} \mathrm{LG}_{p,\ell}^*(r,\phi)E(r,\phi)\mathrm{d}^2 r. \quad (6)$$

This is often achieved using an SLM encoded with the associated phase and amplitude $[\mathrm{LG}_{p,\ell}^*(r,\phi)]$, forming a modal filter. Examples of such phase and amplitudes are shown to the right of the multiplication sign in Fig. 1(b). Taking the Fourier transform thereof allows one to obtain the relation:

$$E_{p,\ell}(k_x, k_y) = \iint_{R^2} \mathrm{LG}_{p,\ell}^*(x,y)E(x,y)e^{-i(k_x x + k_y y)}\mathrm{d}x\,\mathrm{d}y, \quad (7)$$

where (x,y) are the transverse Cartesian coordinates and k_x, k_y are the associated wave vectors. Consideration of the on-axis point, $(k_x, k_y) = (0,0)$, allows the correlation coefficient to be recovered from the equivalence to Eq. (6):

$$C_{p,\ell} = E_{p,\ell}(0,0) = \iint_{R^2} \mathrm{LG}_{p,\ell}^*(x,y)E(x,y)\mathrm{d}x\,\mathrm{d}y. \quad (8)$$

Measurement of the on-axis field then captures the field intensity at that point ($I_{p,\ell}^\rho$), yielding the weighting of that mode:[42]

$$I_{p,\ell}^\rho = |C_{p,\ell}|^2 = |E_{p,\ell}(0,0)|^2. \quad (9)$$

It can be seen that taking the modulus (intensity) eliminates the phase information ($\Delta\varphi$). Subsequent determination of the relative phases is achievable by interfering a reference mode, as described in Ref. 29, among others. Analysis of the generated modes, however, only extended to intensity correlations [Eq. (8)] and thus determination of the phase was not required.

By running the SLM through the basis mode filters and by capturing the corresponding on-axis intensities, the weights ($|C_{p,\ell}|^2 = |\rho_{p,\ell}|^2$) of the summation in Eq. (4) are determined. This decomposes that field into the OAM (ℓ) and radial (p) components present. The fraction of unaltered OAM charge (e.g., $\ell = 0$ in our case for an input Gaussian mode) detected in the decomposition then indicates the conversion efficiency for the light transmitted through the device:

$$\eta_E = 1 - \frac{|C_{0,0}|^2}{\sum_\ell |C_{0,\ell}|^2}. \tag{10}$$

Similarly, the purity (η_P) is then derived from the fraction of OAM detected in the decomposition that corresponds to the value (e.g., $\ell = n$) encoded in the fabricated device:
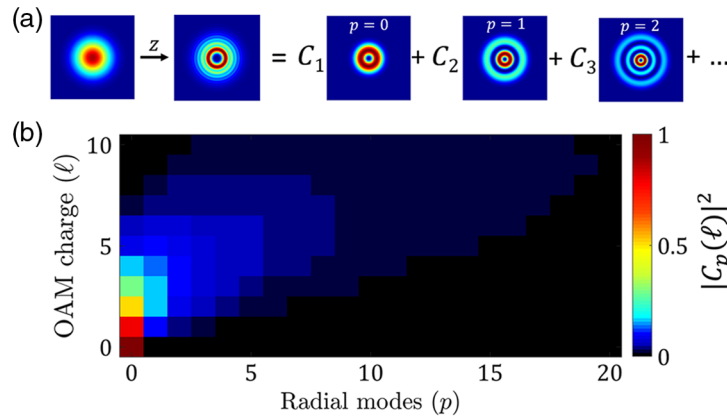
$$\eta_P^n = \frac{|C_{0,n}|^2}{\sum_\ell |C_{0,\ell}|^2}. \tag{11}$$

Accordingly, the conversion efficiency (quantifying the altered light) and purity (quantifying the altered light converted into the desired mode) of the MS may be determined. One is thus able to analyze the losses and modal cross talk altogether. Note that the radial modes are obviated for simplicity in this case ($p = 0$), but the same definition of purity (η_P^n) may also be extended for the p mode basis.

As we are able to also decompose the generated mode into the radial (p) parameter of the LG basis modes, this basis forms a simple platform to fully analyze all the characteristics of the generated mode, allowing one to cover all the possible spatial degrees of freedom. Understanding of the radial characteristics can be achieved by looking at the formulation of the mode produced where incidence of a Gaussian beam profile onto the MS, or any phase-only modulation device, produces a field of the form $E_\ell \propto e^{-(r/w_0)^2} e^{i\ell\phi}$. Clearly, the $|\ell|$-modulated amplitude term ($[r\sqrt{2}/w_0]^{|\ell|}$) in Eq. (5) is absent. As a consequence, the generated modes are not eigenmodes of free space, which, paired with high spatial frequencies near the induced phase singularities, causes the amplitude profile to change dynamics as it propagates along the z axis.[43,44] This is depicted in Fig. 2(a) where the just-modulated Gaussian mode forms rings around the outer profile and an intensity null near the induced singularity.

We can analytically describe such beams, quantifying the effect by a decomposition over the radial terms in the LG basis, $E_\ell = \sum_p C_p \mathrm{LG}_{p,\ell}$, where

$$C_p(\ell) = \sqrt{\frac{(p + |\ell|)!}{p!} \frac{\Gamma(p + \frac{|\ell|}{2})\Gamma(1 + \frac{|\ell|}{2})}{\Gamma(\frac{|\ell|}{2})\Gamma(1 + p + \frac{|\ell|}{2})}} \tag{12}$$


Fig. 2 (a) Observation of phase-only azimuthal modulation of a Gaussian profile produces radial structure and an intensity null near the imparted singularity as it propagates. This equates to a spread of weightings over the radial modes in the LG basis. (b) Simulation of how the radial modal weights with $p = [0,20]$ spread with the imparted OAM charge in the range $\ell = [0,10]$.

are the weighting coefficients for each radial mode, given the imparted charge ℓ and $\Gamma(x)$ is the Gamma function. Plotting Eq. (12) in Fig. 2(b) shows how a spread across the radial modes occurs with this dispersive trend increasing in range and magnitude as the OAM charge increases. Accordingly, the purity of the radial profile ($p = 0$) is reduced when phase-only techniques, such as the JP, are used and the amplitude profile is ignored. It follows that the radial component of the generated modes may also be analyzed with the phase-flattening approach. By then, accounting for the amplitude modulation in the generation step, the undesired radial modes may also be suppressed to yield high purity OAM modes.

Similarly, imparted fractional charges, such as for our fabricated MS, have also been well studied with decomposition into the LG basis analytically described. Considering the fractional charge, expressed as $M = m + \mu$, where m is the integer value and μ is the decimal between 0 and 1, the decomposition into ℓ values is determined by the coefficient[45,46]

$$C_\ell(M) = e^{-i\mu\alpha} \frac{ie^{i(M-\ell)\theta}}{2\pi(M-\ell)} (1 - e^{i2\pi\mu}) e^{i\alpha(m-\ell)}. \tag{13}$$

Here α is the orientation of the fractional edge dislocation with $0 \leq \alpha \leq 2\pi$ and θ indicates the interval $\theta \leq \phi \leq \theta + 2\pi$ for the azimuthal angle where α is measured from. It can be seen that the factional modes are comprised a range of OAM charges which are closest to the nearest integer values of the fractional charge held, as shown in Fig. 3. It may be noted that parameters α and θ affect only the imaginary component, resulting in no changes in the coefficient modulus. As such, only the parameters m and μ are varied in Fig. 3, indicating how the weights of the detected OAM values change for various fractional states. In Fig. 3(a) the integer value is changed between $M = [0.5, 10.5]$, which results in an evenly weighted spread of OAM, decreasing on either side of the fractional charge. This trend remains constant and shifts with m. Alteration of the fractional value μ in Fig. 3(b) then shows an asymmetry in the weights to one side of the adjacent integer charges related to the asymmetry of the fractional value. In Fig. 3(c) a
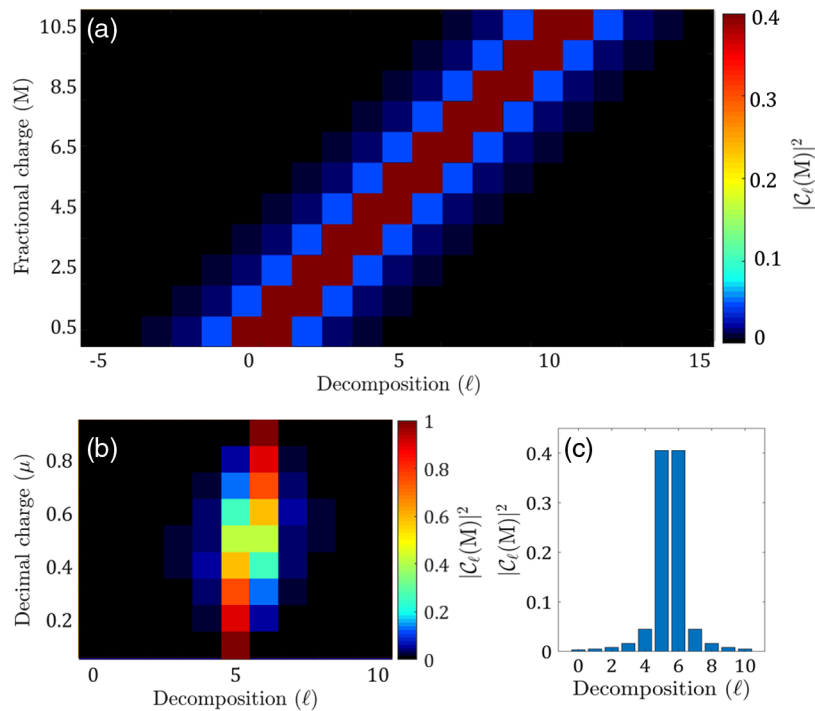
Fig. 3 Depiction of the simulated decomposition spectra of an (a) evenly split decimal value ($\mu = 0.5$) with the integer values spanning $m = [0,10]$ and (b) a variation in the decimal value between $\mu = [0.1, 0.9]$ for integer value $m = 5$. (c) A bar graph of the $\mu = 0.5$ of (b) highlights the spectral trend expected for our fractional device.

bar graph of the spectrum for $M = 5.5$ emphasizes the spectrum for the evenly split decimal value, which was used for our fabricated modes. It follows that quantification of the fractional MS device performance may thus be determined by comparison of the measured decomposition with the calculated distribution.

3 Experimental Setup

Following the concept outlined in Ref. 26, we designed and fabricated MSs for the generation of hybrid OAM states, which may be arbitrarily fashioned in both the paired OAM and polarization bases as described in Sec. 2.1. Here we engineered the dielectric MS from a patterned array of rectangular TiO_2 nano-posts on a fused Si substrate. This is illustrated in Fig. 4(a), in which the consequential manipulation of the horizontal and vertical polarization states was expected to generate $\ell = 1$ and $\ell = 5$ OAM, respectively. Here the width and length (W_x, W_y) was altered to impart different phase delays to traversing light of 532 nm wavelength and the height was kept at 600 nm. Accordingly, particular patterning of the nano-posts with varying width and lengths allows azimuthal phase delays to be imparted on the horizontal, δ_x, and vertical, δ_y, field components as desired in order to engineer a particular phase front related to the incident polarization. Table 1 shows four such MS devices designed to perform hybrid spin-to-OAM conversions, which are tested in this paper where $|H\rangle = [1,0]^T$, $|V\rangle = [0,1]^T$, $|R\rangle = 1/\sqrt{2}[-1, i]^T$ and $|L\rangle = 1/\sqrt{2}[1, i]^T$.

Figure 4(b) shows a microscopic image of JP_3, which generates a 2π azimuthal phase variation for incident horizontal polarization and five 2π azimuthal phase variations for incident vertical polarization. Micrographs from a scanning electron microscope (SEM) are shown on the [Fig. 4(c)] micrometer and [Fig. 4(d)] nanometer scales illustrating the patterning and variation of the nano-post orientations and shapes comprising the device.

Schematics of the experimental setups used in characterizing the MSs are shown in Figs. 5(a) and 5(b). In both setups, a beam of the desired size and OAM was generated through phase and
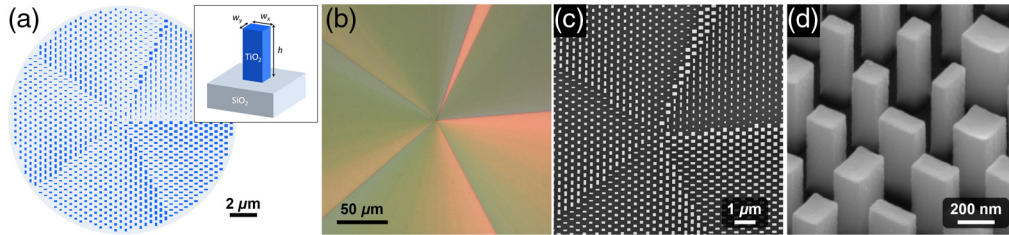

Fig. 4 (a) Exemplary schematic representation of the patterning for JP_3 which allows the generation of helical phase profiles for horizontal and vertical incident polarization states, as detailed in Table 1. The inset details the schematics of a nano-post. (b) Optical microscopic image of the device and SEM micrographs of a section on the device in (c) micrometer and (d) nanometer scales.

Table 1 Table summary of the fabricated MS operations.

MS label	Parameters	Operation on $|H\rangle$ or $|R\rangle$	Operation on $|V\rangle$ or $|L\rangle$
JP_1	$\delta = \pi/2, \chi = \pi/4$ $n = 3, m = 6$	$\widehat{JP_1}|\ell, R\rangle \rightarrow |\ell + 3, L\rangle$	$\widehat{JP_1}|\ell, L\rangle \rightarrow |\ell + 6, R\rangle$
JP_2	$\delta = 0, \chi = 0$ $n = -1, m = 1$	$\widehat{JP_2}|\ell, H\rangle \rightarrow |\ell - 1, H\rangle$	$\widehat{JP_2}|\ell, V\rangle \rightarrow |\ell + 1, V\rangle$
JP_3	$\delta = 0, \chi = 0$ $n = 1, m = 5$	$\widehat{JP_3}|\ell, H\rangle \rightarrow |\ell + 1, H\rangle$	$\widehat{JP_3}|\ell, V\rangle \rightarrow |\ell + 5, V\rangle$
JP_4	$\delta = \pi/2, \chi = \pi/4$ $n = 6.5, m = 3.5$	$\widehat{JP_4}|\ell, R\rangle \rightarrow |\ell + 6.5, L\rangle$	$\widehat{JP_4}|\ell, L\rangle \rightarrow |\ell + 3.5, R\rangle$
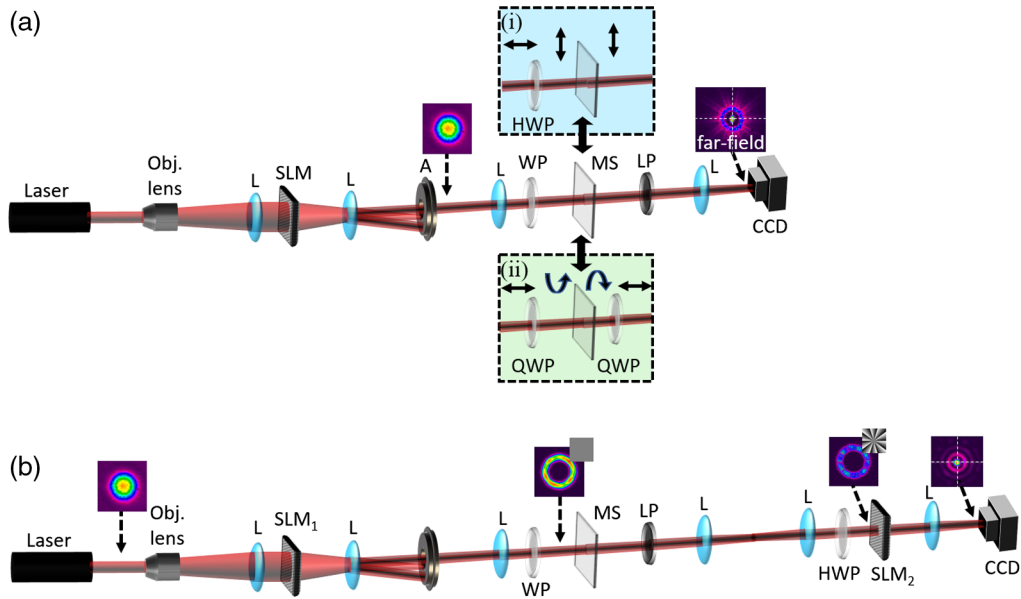
Fig. 5 Illustration of the experimental setup for modal decomposition of the (i) linear and (ii) CP basis JPs in (a) OAM and (b) radial modes. CCD, Charge-coupled device; WP, waveplate; HWP, half-waveplate; QWP, quarter-waveplate; L, lens; LP, linear polarizer; Obj. lens, objective lens; SLM, spatial light modulator; A, aperture; MS, metasurface.

amplitude modulation on an SLM (Holoeye Pluto). Here, a horizontally polarized 532-nm laser was expanded with a $10\times$ objective lens and collimated by a $f = 300$ mm lens to overfill the SLM where an aperture in the Fourier plane of a $4f$ imaging system isolated the first order. The MS was then placed in the image plane of the SLM.

Figure 5(a) depicts the decomposition setup into the $LG_{0,\ell}$ modes with a lens placed a focal length away for measurement of the diffraction-limited central intensity pixels in the Fourier plane with a CCD, yielding the relative intensity coefficients [Eq. (9)]. Insets Figs. 5(i) and 5(ii) illustrate the polarization control for analysis of linear and circular basis MSs, respectively. A half-wave plate (HWP) positioned before the MS altered the linear polarization between horizontal and vertical. A linear polarizer (LP) then projected into horizontal and vertical components. Characterization of the MS in the CP basis required a quarter-waveplate (QWP) positioned before MS to transform linear into CP. Placement of a QWP and LP after the MS then served to project into the right and left CP basis. This formed a "reverse" modal decomposition, equivalent to the relation required in Eq. (6) where the mode sent through the MS was structured to be the filter.

Figure 5(b) illustrates the setup used for decomposition of the generated beam into radial modes as well as control of the incident amplitude profile to eliminate production of radial modes due to the MS phase-only modulation. After structuring the desired amplitude-only profile on SLM_1, the MS-generated mode was imaged onto SLM_2 with a $4f$ system. Here, SLM_2 displayed the desired radial mode filter ($LG_{p,\ell}^*$) and the coefficients similarly measured by a CCD in the Fourier plane of a lens placed focal length away from SLM_2.

4 Results and Discussion

From the operations listed in Table 1, the arbitrary nature of OAM generation is shown where JP_1 was expected to generate $\ell = 3$ for incident right CP and $\ell = 6$ for incident left CP, already exceeding the traditional QP limits where the imparted OAM charges are complex conjugates of the other. By placing JP_1 in the setup described by Fig. 5(a,ii), the mode generated from an incident Gaussian ($\ell = 0$) was decomposed into the $LG_{0,\ell}$ basis where $\ell = [-3,10]$. This was achieved by encoding holograms of the associated complex conjugate modes onto the SLM and selecting the intensities of the diffraction-limited on-axis pixels of the spatial distributions
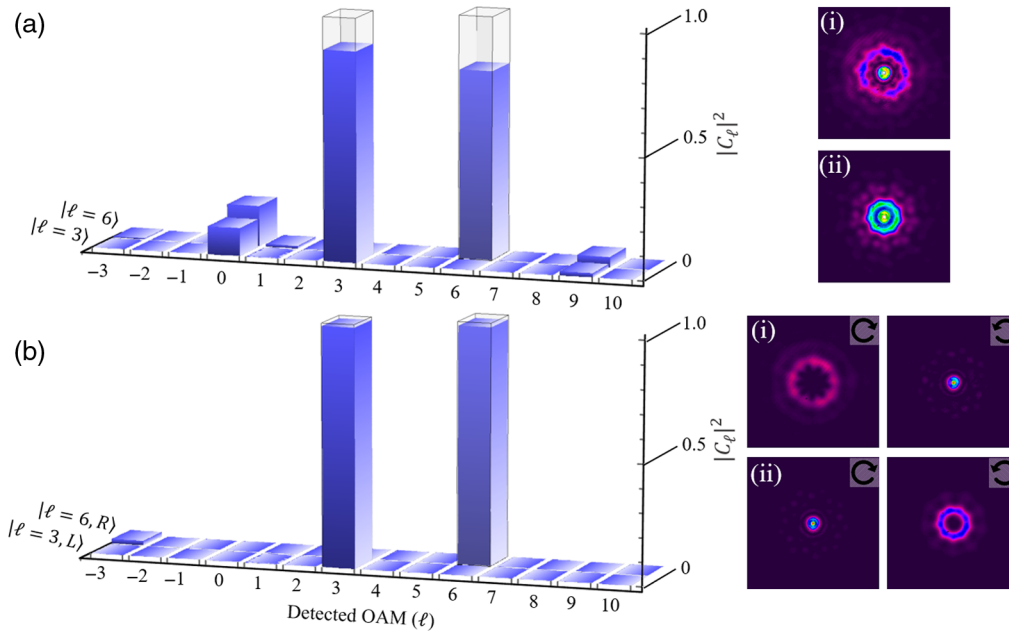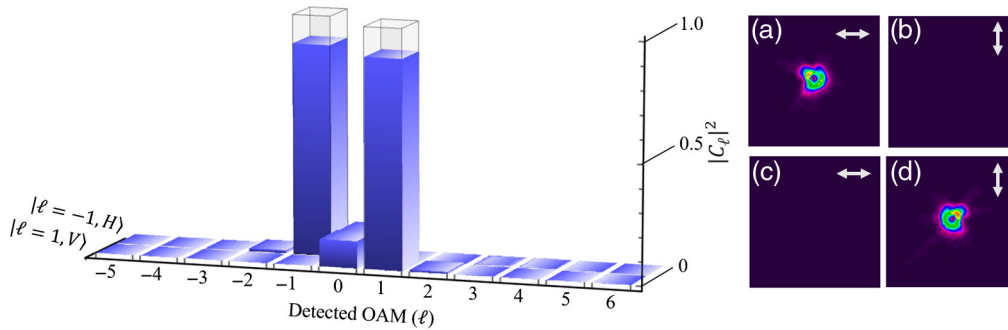
Fig. 6 Experimental results for modal decomposition into the $LG_{0,\ell}$ basis with $\ell = [-3,10]$ for (a) unfiltered and (b) filtered modes generated from JP_1. Clear bars indicate analytically expected results for perfect performance. Insets give the far-field transverse intensity profiles for generated modes (i) $|\ell = 6\rangle$ and (ii) $|\ell = 3\rangle$ with arrows on the top-right corner showing polarization.

recorded in the far field with a CCD. The results are summarized in Fig. 6 where the incident Gaussian with left (right) polarization is given in the back (front) row of the bar graphs in Figs. 6(a) and 6(b). Clear bars show the expected weightings of 1 for perfect mode generation at $\ell = 6$ and $\ell = 3$, respectively. The transverse intensity profiles as seen in the far field are given in insets Fig. 6(i) for $\ell = 6$ and Fig. 6(ii) for $\ell = 3$. Detection of the expected charges is seen with the bars in Fig. 6(a). However, a notable weighting is also seen for the presence of the incident mode, $\ell = 0$. Further analysis of the beam can be seen by looking at the polarization of the modes detected. By using the QWP and LP after the MS, to project the generated mode onto the right and left CP bases, the transverse profiles in Figs. 6(b,i) and 6(b, ii) were seen. Here the ring profile is right CP in (i) while the central Gaussian remains with the original polarization (left CP) and vice versa for (ii). It follows that the Gaussian distribution observed was unconverted by the MS with the weights detected in the decomposition indicating the efficiency of the device according to Eq. (10). Decomposition of the "filtered" modes in the right (left) CP basis for $\ell = 6$ ($\ell = 3$) is given in Fig. 6(b). The purity of the generated beam was thus determined from the fraction of light detected in the designed mode compared to the sum of all the other measured modes. Accordingly, the presence of peaks with 98% and 99% weightings, respectively, show the generation of very pure modes [Eq. (11)]. By substituting the faction of the weighting detected for the Gaussian mode into Eq. (10), a conversion efficiency of 83% and 88% was determined from the unfiltered case. It may be noted that this efficiency does not account for the light lost due to reflection or absorption in the device.

JP$_2$ was expected to generate complex conjugate OAM values of $\ell = \pm 1$ in the linear polarization basis. This subsequently results in a mixed SAM, which is the basis for control, contrary to the pure spin required with QPs. The decomposition here was carried out with the experimental configuration described in Figs. 5(a) and 5(i) where a HWP dictated the linear polarization of the incident Gaussian. Projection of the generated state into the horizontal [Figs. 7(a) and 7(c)] and vertical [Figs. 7(b) and 7(d)] polarization bases show that the polarization remains unchanged in accordance with the operational expectations as linear polarization states form their own complex conjugates. Here the doughnut-like profiles indicate the presence of OAM in both cases.

The decomposition of these modes is given in the bar graph of Fig. 7 over the range $\ell = [-5,5]$. Here high weightings are detected at the expected OAM values of $\ell = -1$ with

Fig. 7 Experimental results for modal decomposition into the $LG_{0,\ell}$ basis with $\ell = [-5,5]$ for modes generated from JP_2. Insets give the far-field transverse intensity profiles for generated modes $|\ell = 6\rangle$ in the horizontal (a) and vertical (b) polarization bases and $|\ell = 3\rangle$ in the horizontal (c) and vertical (d) polarization bases with arrows on the top-right corner showing polarization. Clear bars indicate analytically expected results for perfect performance.

88% for a horizontal polarized input and $\ell = 1$ with 88% for a vertical polarized input. Detection of $\ell = 0$ shows the presence of unconverted light [Eq. (10)] in accordance with the slight off-center positions of the singularities in the transverse profiles.[47,48] As the polarization states of the converted light here remained unaltered, filtration of the unconverted mode was not possible, as was done in the previous case. This is due to the change in polarization of the converted light, allowing it to be separated from the unconverted light with polarization optics. However, as no flip in polarization occurs here, the converted and unconverted light maintain the same polarization and thus cannot be separated accordingly. It follows that while the converted modal purity is high due to the detection of no other modes, the inability to separate the unconverted light results in a modal purity [Eq. (11)] of 88% and a conversion efficiency of 89% for both $\ell = -1$ and $\ell = 1$, reflecting the similar values. It can be noted that the performance of the device for each polarization basis is within less than 1% difference, meaning that the maximum modal cross talk would be lower than -20 dB in the worst case. The operation of JP_3 illustrates the totality of the arbitrary nature by which the MS can be designed where arbitrary OAM can be paired to mixed SAM states. Here the device was expected to yield states of $\ell = 1$ and $\ell = 5$ for incident horizontal and vertical polarization states, respectively. Using the same experimental configuration as for JP_2, the generated modes were decomposed into the OAM range $\ell = [-3,10]$, which is presented in Fig. 8(a). Similarly, due to the linear nature of the polarization basis, it was not possible to filter out the unconverted light. Accordingly, detection of $\ell = 0$ can be seen along with the expected peaks for $\ell = 1$ and $\ell = 5$ in the respective cases. The absence of other detected modes indicate a high degree of purity for the converted light with conversion efficiencies of 96% and 85% being the main source of reduction in purity (96% and 83%). Insets (i) and (ii) of Fig. 8 show the far-field spatial profiles of the beams with the central null in Fig. 8(i) being mostly centralized as the conversion efficiency of the MS here was very high. The greater amount of light in the center of Fig. 8(ii) thus indicates the greater inefficiency for conversion of the mode into $\ell = 5$, showing also slightly higher modal cross talk with the neighboring modes.

Here we also consider the radial purity of the $\ell = 5$ mode, in comparison to Eq. (12), by decomposition into the $LG_{p,5}$ basis with the filter beam waist equated to that of the incident Gaussian. This was carried out with setup Fig. 5(b) where SLM_1 was used to structure the appropriate-sized Gaussian as illustrated in inset Fig. 8(b, iii), yielding the modal structure seen in Fig. 8(b, iv) with a flat phase front. The generated mode was then decomposed with radial mode filters displayed on SLM_2 where $p = [0,10]$. Excellent agreement can be seen between the predicted and measured values with a similarity of over 99%. It follows that the nature of the radial spread is equivalent to that of the modes generated by other phase-only devices. Here a substantial spread is seen over all 10 measured modes with only 15% of the measured weights remaining in the desired $p = 0$ mode and the dominant radial mode moved outward to $p = 1$ with a 16% contribution. Such radial contributions, or purity, can be extracted from Eq. (11), considering a fixed OAM now ($\ell = 5$) and performing a similar
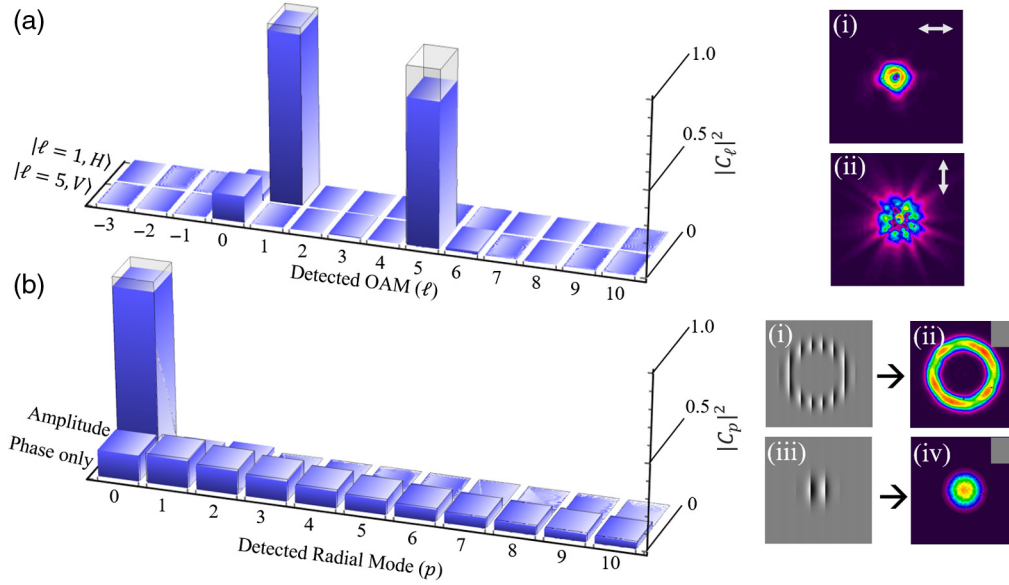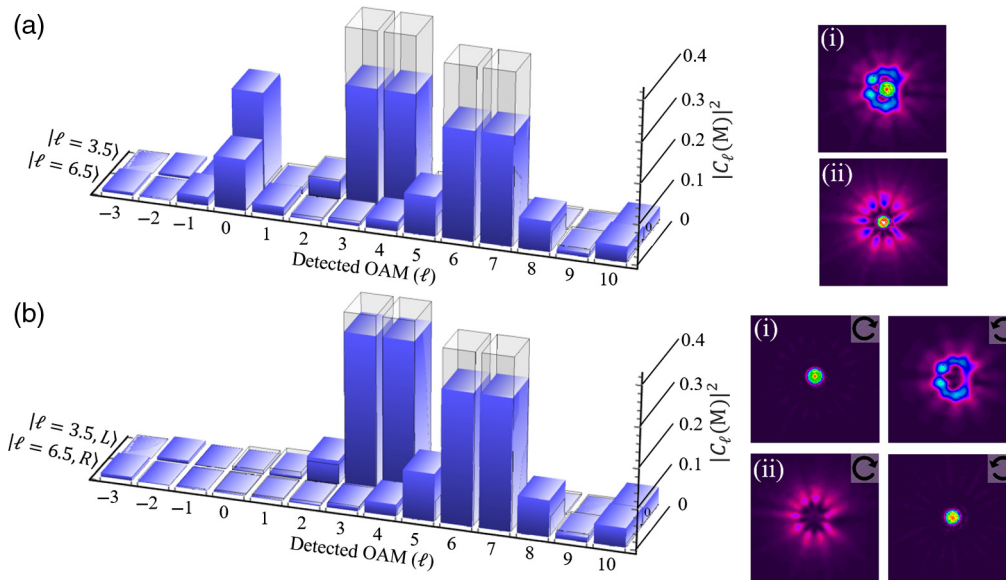
Fig. 8 Experimental results for modal decomposition into the (a) $LG_{0,\ell}$ basis where $\ell = [-5,5]$ for modes generated from JP_3 with the far-field transverse intensity profiles of (i) $|\ell = 1\rangle$ in the horizontal polarization basis and (ii) $|\ell = 5\rangle$ in the vertical polarization basis. Arrows on the top-right corner show polarization. Experimental decomposition into (b) the $LG_{p,5}$ basis with $p = [0,10]$ for the $\ell = 5$ mode with the (i) $|\ell|$-modulated ring holograms generating a (ii) flat phase-front ring profile and (iii) a Gaussian hologram generating a (iv) flat phase-front ring profile. Grayscale images on the top-right corner indicate encoded phase profiles and the clear bars indicate analytically expected results for perfect performance. The radial mode results are normalized over the detection range.

decomposition along the radial modes $\eta_P^r = |C_{r,5}|^2 / \sum_p |C_{p,5}|^2$, where r is the radial mode being characterized.

By additionally structuring the amplitude of the light incident onto the MS into a $|\ell|$-dependent doughnut profile shown in Fig. 8(b,ii), we also show that it is possible to remove this phase-only modulation effect. Here Fig. 8(b,i) shows the hologram displayed on SLM_1 where the phase-profile remains flat. As can be seen in the decomposition spectrum, when the amplitude structure is also catered for as described in Ref. 43, the radial profile is contained in the $p = 0$ mode resulting in a measured 95% purity compared to the 15% detected previously.

However, OAM generation with these hybrid devices are not only restricted to integer charges, but it may also be extended to the fractional regime as expected for the operation of JP_4 in Table 1. As the polarization basis is circular, the MS was analyzed with the setup in Fig. 5(a,ii). The decomposition performed without filtering the unconverted light is shown in Fig. 5(a) for the $\ell = 3.5$ and $\ell = 6.5$ with right and left CP inputs, respectively. Following the expected decomposition spectrum provided by Eq. (13), which is shown by the clear bars, an even spread between the closest OAM modes is expected, which continues outward with a steep drop-off in the weightings on either side. Here, the parameters used in Eq. (13) were $\mu = 0.5$, $\alpha = \pi/2$, and $\theta = -\pi/2$. This trend is also seen in Fig. 9(a) with the additional presence of $\ell = 0$ due to the unconverted modal contribution. Subsequently, a conversion efficiency of 76% (83%) for $\ell = 3.5$ ($\ell = 6.5$) was calculated. Consequently, the spatial profiles yielded intensity in the center of the ring. It may be noted that a characteristic null along a side of both of the outer rings for $\ell = 3.5$ and $\ell = 6.5$ reflects the fractional nature of the charge being carried. Using the change in polarization for CP-generated modes to filter the unconverted light, the decomposition performed on the modulated light is shown in Fig. 9. Here, insets Figs. 9(b,i) and 9(b,ii) show projections of the modes based on the polarization. The OAM spectrum detected here is similar to the simulated cases; however, the peak modal weights are slightly lower and the device also generated 3.5% (4%) of $\ell = 10$ alongside the fractional charge spectrum for $\ell = 3.5$ ($\ell = 6.5$). The appearance of such undesired higher OAM modes could possibly be due to the complexity

Fig. 9 Experimental results for modal decomposition into the $LG_{0,\ell}$ basis with $\ell = [-3,10]$ for (a) unfiltered and (b) filtered modes generated from JP_4. Clear bars indicate numerically expected results [Eq. (13)] for perfect performance. Insets give the far-field transverse intensity profiles for generated modes (i) $|\ell = 3.5\rangle$ and (ii) $|\ell = 6.5\rangle$ with arrows on the top-right corner showing polarization.

of the design where for these fractional modes, there is a line on the JP that yields a phase jump of π across it, resulting in the destructive interference and a nonuniform field in the far field. However, this still requires further studies in future MS designs. It follows that while the purity of the state is reduced by 4% from the conversion efficiency, 72% (79%), it still remains relatively high if compared with the expected purity, 78% (82%), calculated from the theoretically simulated OAM spectrum shown in Fig. 3(a). Here the decreased conversion efficiency in comparison to the other devices may also be a result of the design complexity, but further studies are needed for definitive explanations thereof.

5 Conclusion

With the myriad of applications for OAM containing light, including those requiring polarization as a control for the generation, it follows that the purity of the generated modes is of substantial significance for high fidelity outcomes. Similarly, ease of generation and flexibility of what values in degrees of freedom may be used (i.e., polarization and OAM modes) is of interest. As such, we have fabricated MS elements that exploit a total spin-to-OAM conversion, allowing freedom in both the OAM charges, including fractional values, produced in a single device, as well as the incident polarization basis by which the charges may be generated.

We additionally employed a phase-flattening approach to analyze the performance of these devices and decompose the generated beams into a known modal basis, illustrating this technique as a convenient and quantitative method by which both the purity and the efficiency of such devices can be determined. Good performances of the devices were found with the lowest conversion efficiency not falling below 75%, despite highly complex designs. Here the presence of unconverted light could be explained from the nonideal transmission and phase of the selected nano-posts, limited by the finite possibility of its dimensions. In addition, higher-order momentum conversion also theoretically results in less conversion efficiency and another significant factor may be error between the fabricated and the designed nano-post dimensions. Compared to other recently reported visible MS-based Pancharatnam–Berry devices, this device indicates good performance in this regard with reported values ranging from 70%[49] to 90%.[50]

A high fidelity was also shown for our devices where no additional modes were generated alongside the engineered and unconverted charges with the nonfractional JPs. For the fractional

case, the impurity of the generated modes was very low with only 4% of an extraneous mode being additionally generated. Furthermore, similarity to the predicted decomposition spectrum exceeded 78% with the unconverted light being filtered out.

Another distinct advantage shown for decomposition as an analysis technique is the ability to then fully determine the dynamics of the beam as the properties of the basis modes are well known. As was shown in case of expansion into the radial mode basis for $\ell = 5$, a wide spread into higher radial modes was seen accompanying a substantial reduction in the power remaining in the often-desired $p = 0$ mode. With this characterization, we also illustrate how to compensate for this effect by controlling the amplitude degree of freedom in the generation step, containing the generated mode within the desired $p = 0$ mode.

Acknowledgments

References

1. L. Allen et al., "Orbital angular momentum of light and the transformation of Laguerre–Gaussian laser modes," *Phys. Rev. A* **45**(11), 8185–8189 (1992).
2. J. Wang et al., "Terabit free-space data transmission employing orbital angular momentum multiplexing," *Nat. Photonics* **6**(7), 488–496 (2012).
3. G. Gibson et al., "Free-space information transfer using light beams carrying orbital angular momentum," *Opt. Express* **12**, 5448–5456 (2004).
4. J. Shapiro, S. Guha, and B. Erkmen, "Ultimate channel capacity of free-space optical communications," *J. Opt. Networking* **4**(8), 501–516 (2005).
5. M. Mafu et al., "Higher-dimensional orbital-angular-momentum-based quantum key distribution with mutually unbiased bases," *Phys. Rev. A* **88**(3), 032305 (2013).
6. K. Toyoda et al., "Using optical vortex to control the chirality of twisted metal nanostructures," *Nano Lett.* **12**(7), 3645–3649 (2012).
7. K. Toyoda et al., "Transfer of light helicity to nanostructures," *Phys. Rev. Lett.* **110**, 143603 (2013).
8. J. Lee et al., "Photopolymerization with light fields possessing orbital angular momentum: generation of helical microfibers," *ACS Photonics* **5**(10), 4156–4163 (2018).
9. B. Roxworthy and K. Toussaint, "Optical trapping with π-phase cylindrical vector beams," *New J. Phys.* **12**, 073012 (2010).
10. M. G. Donato et al., "Optical trapping of nanotubes with cylindrical vector beams," *Opt. Lett.* **37**, 3381–3383 (2012).
11. A. Abouraddy and K. Toussaint, "Three-dimensional polarization control in microscopy," *Phys. Rev. Lett.* **96**, 153901 (2006).
12. Q. Zhan, "Cylindrical vector beams: from mathematical concepts to applications," *Adv. Opt. Photonics* **1**, 1–57 (2009).
13. F. Cardano et al., "Quantum walks and wavepacket dynamics on a lattice with twisted photons," *Sci. Adv.* **1**(2), e1500087 (2015).
14. B. Sephton et al., "A versatile quantum walk resonator with bright classical light," *PLoS One* **14**(4), e0214891 (2019).
15. B. Ndagano et al., "Characterizing quantum channels with non-separable states of classical light," *Nat. Phys.* **13**(4), 397–402 (2017).
16. V. Parigi et al., "Storage and retrieval of vector beams of light in a multiple-degree-of-freedom quantum memory," *Nat. Commun.* **6**, 7706 (2015).
17. S. Khonina et al., "The phase rotor filter," *J. Mod. Opt.* **39**(5), 1147–1154 (1992).
18. Y. Ohtake et al., "Universal generation of higher-order multiringed Laguerre–Gaussian beams by using a spatial light modulator," *Opt. Lett.* **32**, 1411–1413 (2007).
19. T. Ando et al., "Mode purities of Laguerre–Gaussian beams generated via complex-amplitude modulation using phase-only spatial light modulators," *Opt. Lett.* **34**(1), 34–36 (2009).

20. L. Marrucci, C. Manzo, and D. Paparo, "Optical spin-to-orbital angular momentum conversion in inhomogeneous anisotropic media," *Phys. Rev. Lett.* **96**, 163905 (2006).
21. F. Bouchard et al., "Optical spin-to-orbital angular momentum conversion in ultra-thin meta-surfaces with arbitrary topological charges," *Appl. Phys. Lett.* **105**(10), 101905 (2014).
22. E. Karimi et al., "Generating optical orbital angular momentum at visible wavelengths using a plasmonic metasurface," *Light Sci. Appl.* **3**(5), e167 (2014).
23. M. Kang et al., "Wave front engineering from an array of thin aperture antennas," *Opt. Express* **20**(14), 15882–15890 (2012).
24. G. Li et al., "Spin-enabled plasmonic metasurfaces for manipulating orbital angular momentum of light," *Nano Lett.* **13**(9), 4148–4151 (2013).
25. R. C. Devlin et al., "Spin-to-orbital angular momentum conversion in dielectric metasurfaces," *Opt. Express* **25**(1), 377–393 (2017).
26. R. C. Devlin et al., "Arbitrary spin-to–orbital angular momentum conversion of light," *Science* **358**(6365), 896–901 (2017).
27. J. Yao et al., "Investigation of damage threshold to TiO_2 coatings at different laser wavelength and pulse duration," *Thin Solid Films* **516**(6), 1237–1241 (2008).
28. D. Flamm et al., "All-digital holographic tool for mode excitation and analysis in optical fibers," *J. Lightwave Technol.* **31**(7), 1023–1032 (2013).
29. T. Kaiser et al., "Complete modal decomposition for optical fibers using CGH-based correlation filters," *Opt. Express* **17**, 9347–9356 (2009).
30. I. A. Litvin et al., "Azimuthal decomposition with digital holograms," *Opt. Express* **20**(10), 10996–11004 (2012).
31. C. Schulze et al., "Modal decomposition without a priori scale information," *Opt. Express* **20**, 27866–27873 (2012).
32. G. Ruffato, M. Massari, and F. Romanato, "Multiplication and division of the orbital angular momentum of light with diffractive transformation optics," *Light Sci. Appl.* **8**, 113 (2019).
33. T. Omatsu et al., "Metal microneedle fabrication using twisted light with spin," *Opt. Express* **18**(17), 17967–17973 (2010).
34. Y. Yang et al., "Dielectric meta-reflectarray for broadband linear polarization conversion and optical vortex generation," *Nano Lett.* **14**(3), 1394–1399 (2014).
35. T. Omatsu, K. Miyamoto, and A. J. Lee, "Wavelength-versatile optical vortex lasers," *J. Opt.* **19**(12), 123002 (2017).
36. A. Forbes, "Controlling light's helicity at the source: orbital angular momentum states from lasers," *Philos. Trans. R. Soc. London Ser. A* **375**(2087), 20150436 (2017).
37. D. Naidoo et al., "Controlled generation of higher-order Poincaré sphere beams from a laser," *Nat. Photonics* **10**(5), 327–332 (2016).
38. X. Wang et al., "Recent advances on optical vortex generation," *Nanophotonics* **7**(9), 1533–1556 (2018).
39. S. Pancharatnam, "Generalized theory of interference and its applications—part II. Partially coherent pencils," *Proc. Indian Acad. Sci. Sec. A* **44**, 398–417 (1956).
40. M. V. Berry, "Quantal phase factors accompanying adiabatic changes," *Proc. R. Soc. London Ser. A* **392**(1802), 45–57 (1984).
41. Z. Bomzon, V. Kleiner, and E. Hasman, "Pancharatnam–Berry phase in space-variant polarization-state manipulations with subwavelength gratings," *Opt. Lett.* **26**(18), 1424–1426 (2001).
42. A. Forbes, A. Dudley, and M. McLaren, "Creation and detection of optical modes with spatial light modulators," *Adv. Opt. Photonics* **8**(2), 200–227 (2016).
43. B. Sephton, A. Dudley, and A. Forbes, "Revealing the radial modes in vortex beams," *Appl. Opt.* **55**(28), 7830–7835 (2016).
44. E. Karimi et al., "Hypergeometric-Gaussian modes," *Opt. Lett.* **32**(21), 3053–3055 (2007).
45. J. B. Götte et al., "Quantum formulation of fractional orbital angular momentum," *J. Mod. Opt.* **54**(12), 1723–1738 (2007).
46. J. B. Götte et al., "Light beams with fractional orbital angular momentum and their vortex structure," *Opt. Express* **16**(2), 993–1006 (2008).

47. A. Mair et al., "Entanglement of the orbital angular momentum states of photons," *Nature* **412**, 313–316 (2001).

48. A. Vaziri, G. Weihs, and A. Zeilinger, "Superpositions of the orbital angular momentum for applications in quantum experiments," *J. Opt. B* **4**(2), S47 (2002).

49. R. Xie et al., "High-efficiency ultrathin dual-wavelength Pancharatnam-Berry metasurfaces with complete independent phase control," *Adv. Opt. Mater.* **7**(20), 1900594 (2019).

50. J. Zhou et al., "Optical edge detection based on high-efficiency dielectric metasurface," *Proc. Natl. Acad. Sci. U.S.A.* **116**(23), 11137–11140 (2019).

Bereneice Sephton recieved her BSc and honors degrees from Nelson Mandela Metropolitan University before joining CSIR as MSc student researcher in 2016 and completing her MSc degree with the University of the Witwatersrand in Quantum Walks in 2018. Currently, she is pursuing her PhD in the Structured Light Group there, where she is using the properties of structured light to implement quantum teleporation.

Yao-Wei Huang received his BS degree in optics and photonics from National Central University in 2010, and his MS and PhD degrees with dean's awards in applied physics from National Taiwan University, respectively in 2012 and 2015. He has been a postdoctoral fellow at Harvard University since 2017 and a research fellow at the National University of Singapore since 2016. His research interests include nanophotonics, metasurfaces, structured light, bio-medical optics, and computational imaging.

Antonio Ambrosio has been a principal scientist at the Center for Nanoscale Systems at Harvard University since July 2016. Since September 2019, he has been PI of the research line named vectorial nanoimaging at the Center for Nano Science and Technology (CNST) of IIT in Milan, dedicated to the development of metasurface-based optical nanodevices and new optical near-field imaging and spectroscopy techniques for 2-D materials, polymers, and nanostructured surfaces.

Adam Vallés received his BSc degree in telecom engineering at the Polytechnic University of Catalonia before changing his field with an MSc degree in quantum optics and a PhD that involved studying the relation between entanglement, Bell's inequalities, and coherence at the Institute of Photonic Sciences (ICFO). He was awarded as postdoctoral fellowship and joined the Structured Light Group at the University of the Witwatersrand and now is currently working as an assistant professor at Chiba University.

Takashige Omatsu received his PhD from the University of Tokyo in 1992, and he was appointed as a professor at Chiba University in 2007. He has been developing structured light sources and pioneering structured light materials processing. Currently, he is playing a role as an editor-in-chief, *OSA Continuum*, OSA Publishing. He was elected as OSA fellow, SPIE fellow, and JSAP fellow.

Andrew Forbes received his PhD from the University of Natal, South Africa, in 1998 and subsequently spent several years as an applied laser physicist, first in a technology start-up where he was technical director, then as a chief researcher and research group leader at the CSIR. He is a distinguished professor within the U. Witwatersrand, South Africa, where he has established a new laboratory for structured light. He is a fellow of SPIE and OSA.

Biographies of the other authors are not available.